Superconductivity in metallic twisted bilayer graphene stabilized by WSe$_2$

Harpreet Singh Arora[1,2*], Robert Polski[1,2*], Yiran Zhang[1,2,3*], Alex Thomson[2,3,4], Youngjoon Choi[1,2,3], Hyunjin Kim[1,2,3], Zhong Lin[5], Ilham Zaky Wilson[5], Xiaodong Xu[5,6], Jiun-Haw Chu[5], Kenji Watanabe[7], Takashi Taniguchi[7], Jason Alicea[2,3,4] and Stevan Nadj-Perge[1,2†]

[1]*T. J. Watson Laboratory of Applied Physics, California Institute of Technology, 1200 East California Boulevard, Pasadena, California 91125, USA*
[2]*Institute for Quantum Information and Matter, California Institute of Technology, Pasadena, California 91125, USA*
[3]*Department of Physics, California Institute of Technology, Pasadena, California 91125, USA*
[4]*Walter Burke Institute for Theoretical Physics, California Institute of Technology, Pasadena, California 91125, USA*
[5]*Department of Physics, University of Washington, Seattle, Washington 98195, USA*
[6]*Department of Materials Science and Engineering, University of Washington, Seattle, WA 98195, USA*
[7]*National Institute for Materials Science, Namiki 1-1, Tsukuba, Ibaraki 305 0044, Japan*
*These authors contributed equally to this work
[†]*Correspondence: s.nadj-perge@caltech.edu*

Magic-angle twisted bilayer graphene (TBG), with rotational misalignment close to 1.1°, features isolated flat electronic bands that host a rich phase diagram of correlated insulating, superconducting, ferromagnetic, and topological phases.[1–6] Both correlated insulators and superconductivity have been previously observed only for angles within ±0.1° from the magic-angle value and occur in adjacent or overlapping electron-density ranges; nevertheless, the origins of these states and the relation between them remain particularly elusive due to their sensitivity to microscopic details. Beyond twist angle and strain, the dependence of the TBG phase diagram on the alignment[4,6] and thickness of insulating hexagonal boron nitride (hBN)[7,8] used to encapsulate the graphene sheets indicates the importance of the microscopic dielectric environment. Here we show that adding an insulating tungstendiselenide (WSe$_2$) monolayer between hBN and TBG stabilises superconductivity at twist angles much smaller than the magic-angle value. For the smallest angle of $\theta = 0.79°$, we still observe superconductivity, despite TBG exhibiting metallic behaviour across the whole range of electron densities. Finite-magnetic-field measurements further reveal weak antilocalization signatures as well as breaking of four-fold spin-valley symmetry, consistent with spin-orbit coupling induced in TBG via proximity to WSe$_2$. Our results strongly constrain theoretical explanations for the emergence of superconductivity in TBG and open new avenues for engineering quantum phases in moiré systems.

Strongly correlated electron systems often exhibit a variety of quantum phases with similar ground-state energies, separated by phase boundaries that depend sensitively on microscopic details. Twisted

bilayer graphene, with twist angle close to the magic angle $\theta_M \approx 1.1°$, has recently emerged as a highly tunable platform with an exceptionally rich phase diagram[1,2] hosting correlated insulating states, superconductivity, and ferromagnetism.[3–6] Strong correlations in TBG originate from the non-dispersive (flat) bands that are created by the hybridization of the graphene sheets[9] and are isolated from the rest of the energy spectrum by an energy gap ~ 30 meV.[10,11] Previous transport experiments on magic-angle TBG found that the correlated insulators are often accompanied by superconductivity in a narrow range $\pm 0.1°$ around θ_M,[1,3,7,8,12] with signatures of these states observed down to $0.93°$.[13] Close to θ_M, the correlated insulators develop at electron densities that correspond to an integer number ν of electrons per moiré unit cell and are surrounded by intermittent pockets of superconductivity;[5] both phases appear most frequently around $\nu = \pm 2$.[2,3] Away from θ_M, however, both phases are suppressed as the effects of electron-electron interactions quickly diminish due to a rapid increase of the flat-band bandwidth and corresponding dominance of kinetic energy.[1,9] In addition to the TBG twist angle, the physics of the correlated phases is also affected by the hBN employed as a high-quality dielectric. In particular, since hBN and graphene exhibit similar crystal lattices, the relative alignment between the hBN and TBG is critical. For example, a ferromagnetic state near $\nu = +3$ was observed in devices where hBN aligns with TBG.[4,6] However, in such devices the band structure of the flat bands is strongly altered,[6] and superconductivity—typically observed when hBN and TBG are misaligned—is absent. Recent work using a very thin hBN layer separating a back gate from TBG additionally suggests that electrostatic screening plays a role in the appearance of insulating and superconducting states[7] (see also Ref. 8). These experiments exemplify the effects of hBN layers on the phase diagram in hBN-TBG-hBN structures and highlight the importance of understanding how microscopic details of the dielectric environment alter the properties of correlated phases.

Here, instead of the usual hBN-TBG-hBN structures, we investigate devices made from hBN-TBG-WSe$_2$-hBN van der Waals stacks in which a monolayer of WSe$_2$ resides between the top hBN and TBG (Fig. 1a). Our stacks are assembled using a modified 'tear and stack' technique where the 'tearing' and 'stacking' of TBG is facilitated by monolayer WSe$_2$; see Methods and Extended Data Fig. 1 for fabrication details. Like hBN, flakes of transition metal dichalcogenides, such as WSe$_2$, can be used as high-quality insulating dielectrics for graphene-based devices;[14] however, the two van der Waals dielectrics differ in several ways that may alter the TBG band structure. First, unlike hBN, the WSe$_2$ and graphene lattice constants differ significantly (0.353 nm for WSe$_2$ and 0.246 nm for graphene, Fig. 1b). This mismatch implies that the moiré pattern formed between TBG and WSe$_2$ has a maximum lattice constant ~ 1 nm—much smaller than that formed in small-angle TBG (> 10 nm). Second, it is well-established that WSe$_2$ can induce a spin-orbit interaction (SOI) in graphene via van der Waals proximity.[15–18] And finally, due to hybridization effects, WSe$_2$ may also change both the Fermi velocity of the proximitized graphene sheet and the system's phonon spectrum. We chose to use monolayer WSe$_2$ in particular because of its large band gap[19] that allows applying a large range of gate voltages. It has also been suggested previously that a monolayer induces larger spin-orbit coupling in graphene compared to few-layer WSe$_2$.[18]

2

We have studied four TBG-WSe$_2$ devices and show results for two of them in the main text (see Extended Data Fig. 4 and Extended Data Fig. 7 for data from two additional devices). Surprisingly, we find robust superconductivity in all studied TBG-WSe$_2$ structures, even for twist angles far outside of the previously established range. Figures 1c-e show the temperature dependence of resistance over three TBG regions corresponding to angles $\theta = 0.97°$, $\theta = 0.87°$ and $\theta = 0.79°$ (see Methods for details about twist-angle determination); in all cases superconducting transitions are clearly visible. Aside from the drop in longitudinal resistance (R$_{xx}$) to zero, we also observe well-resolved Fraunhofer-like patterns for all three angles (Figs. 1f-h), qualitatively similar to the typical hBN-TBG-hBN devices.[2,3,5] The small periodic modulations of the critical current in magnetic field have been previously attributed to the presence of Josephson junctions in the system, independently corroborating the presence of superconducting correlations. In our devices, we typically see periods of 1.5-3 mT that, if interpreted as the effective junction area $S \sim 0.67–1.33 \, \mu m^2$, are consistent with the device geometry.

For the largest angle $\theta = 0.97°$, a superconducting pocket emerges on the hole side near $\nu = –2$ with a maximal transition temperature T$_c \approx 0.8$ K. To our knowledge, this is the smallest angle for which superconductivity has been reported for hole doping. Careful inspection reveals another weak superconductivity pocket close to $\nu = +2$ (the behavior at low fields is displayed in Extended Data Fig. 6). However, despite the small twist angle—falling outside the $\theta_{\mathrm{M}} \pm 0.1°$ range— the observed phase diagram resembles that of regular high-quality magic-angle hBN-TBG-hBN structures.[2,5] For this angle, correlated insulating states are also observed for filling factors $\nu = +2$, +3 with activation gaps of $\Delta_{+2} = 0.68$ meV and $\Delta_{+3} = 0.08$ meV, whereas at other filling factors correlated states are less developed and do not show insulating behavior (see Fig. 2f and Extended Data Fig. 3).

Although superconductivity persists for all three angles, the correlated insulators are quickly suppressed as the twist angle is reduced. This suppression is not surprising, as for angles below θ_{M}, the bandwidth increases rapidly and, moreover, the characteristic correlation energy scale $e^2/4\pi\epsilon L_m$ also diminishes due to an increase in the moiré periodicity $L_m = a/\sin(\theta/2)$ ($a = 0.246$ nm denotes the graphene lattice constant).[1,9,10,20–22] For the lower angle of $\theta = 0.87°$ correlated-insulating behavior is heavily suppressed at all filling factors. In Fig. 1d, a peak in longitudinal resistance versus density is visible only around $\nu = +2$ above the superconducting transition ($T_c = 600–800$ mK). Data for a larger temperature range (Fig. 2a-b) shows that the resistance peak near $\nu = +2$ survives up to $T = 30$ K, and also reveals a new peak near $\nu = +1$ in the temperature range 10-35 K. These observations suggest that electron correlations remain strong, though the corresponding states appear to be metallic as the overall resistance increases with temperature. For this angle, we measure activation gaps at full filling (i.e., at $\nu = \pm4$) of $\Delta_{+4} = 8.3$ meV and $\Delta_{-4} = 2.8$ meV (Fig. 2e) —far smaller than the gaps around θ_{M}, in line with previous results that report a disappearance of the band gap separating dispersive and flat bands at around $\theta = 0.8°$.[11,23]

Indeed, at the smallest angle, $\theta = 0.79°$, along with the lack of insulating states at any partial filling, the resistance at full filling is even more reduced (Figs. 2c-d). The relatively low resistances

3

< 2 kΩ, measured at full filling—which are less than 15% of the resistance at the charge neutrality point (CNP)—suggest a semi-metallic band structure around full filling, consistent with theoretical expectations for TBG at $\theta = 0.79°$[23] and the resistivity of a dilute 2D electron gas.[24] Surprisingly, despite the complete absence of both full-filling band gaps and correlated insulators, the superconducting low-resistance pocket near $\nu = +2$ is clearly resolved (Figs. 1e, h; see also Extended Data Fig. 7 for confirmation in a second device at $0.80°$).

Both the disappearance of the correlated insulators and the vanishing gap between flat and dispersive bands for low angles suggest that the additional WSe$_2$ monolayer does not significantly change the magic angle (on the scale of angles considered here). Since superconductivity survives at much lower angles than the correlated insulating states, our observations strongly suggest the two phenomena have different origins.[7,8] Note also that the close proximity of the dispersive bands does not seem to have a major impact on the superconducting phase. Our findings of superconductivity in TBG with metallic band structure put strong constrains on the proposed theoretical explanations and are the main result of this work. For example, our observations are in contrast with scenarios wherein superconductivity descends from a Mott-like insulating state as in high-T_c superconductors[25] and more consistent with phonon-only mediated superconductivity.[26–28] We emphasise, however, that electron correlations may still prove important for the development of superconductivity. For instance, even for the smallest angle of $\theta = 0.79°$, the superconducting pocket is seemingly pinned to the vicinity of $\nu = 2$. Additionally, as shown in Fig. 2, at higher temperatures residual R$_{xx}$ peaks can still appear at certain integer filling factors despite the absence of gapped correlated insulating states. It is thus hard to rule out the possibility that superconductivity arises from correlated states of metallic nature that may be present at smaller angles and near integer values of ν in analogy to other exotic superconducting systems.[29–31]

Measurements in finite magnetic field reveal further insights into the physics of TBG-WSe$_2$ structures (Fig. 3). First, in small fields we observe a conductance peak at $B = 0$ mT, indicative of weak antilocalization and consequently the presence of strong SOI (see Extended Data Fig. 8). Previous works established that WSe$_2$ can induce large SOI into monolayer and bilayer graphene,[16–18] and hence the generation of SOI in the proximitized layer of TBG is expected. Second, surprisingly, for all three angles we find that even at modest magnetic fields, above $B = 1$ T, gaps between Landau levels are well-resolved, showing a fan diagram that diverges from the CNP. The slopes of the dominant sequence of R$_{xx}$ minima correspond to even-integer Landau level fillings ± 2, ± 4, ± 6, etc.—indicating broken four-fold (spin-valley flavor) symmetry. By contrast, the majority of previous transport experiments[2,3,5,7,8,13,32] near the magic angle report a Landau-fan sequence ± 4, ± 8, ± 12 at the CNP, with broken-symmetry states being only occasionally observed at the lowest Landau level (corresponding to the ± 2 sequence).[4,5,32] In addition to R$_{xx}$ minima corresponding to the gaps between Landau levels, we also measured quantized Hall conductance plateaus, further corroborating the two-fold symmetry and indicating the low disorder in the measured TBG areas. Note also that for the smallest angle ($\theta = 0.79°$) we do not observe obvious signatures of correlated insulating states near $\nu = 2$ up to $B = 4$ T.

4

The observation of additional Landau levels is also consistent with a scenario in which the TBG band structure is modified by SOI inherited from the WSe_2 monolayer. Continuum-model calculations (Fig. 4; see also Extended Data Fig. 10 and Supplementary Information section I) taking into account this effect show that the presence of SOI, regardless of specific details, lifts the degeneracy of both flat and dispersive bands, thereby breaking four-fold spin-valley symmetry. In a finite magnetic field, the resulting Landau levels then descend from two-fold degenerate Kramers states (see corresponding discussion in Supplementary Information section II). We emphasise that the fan diagram has been reproduced in multiple samples—including a device with WSe_2 on both the top and bottom (D4, 0.80°, Extended Data Fig. 7, which also shows a very similar temperature dependence to the 0.79° area in D2). The latter observation indicates that mirror symmetry breaking by WSe_2 placed on only one side of the TBG does not account for the observed degeneracy lifting. Odd steps—which are not generated by the SOI—are occasionally observed for low angles (green dashed lines in Fig. 3). We attribute these steps to additional symmetry breaking, possibly due to correlation effects originating either from flat-band physics or simply a magnetic-field-induced effect (e.g., Zeeman splitting or exchange interaction) at low electronic densities. Moreover, our data reveal an apparent recurrence of 4-fold degeneracy for large Landau-level fillings, ±14, ±18, ±22, which are still offset from the usual sequence of ±16, ±20, ±24 (Fig. 3c and Extended Data Fig. 5). The mechanism of SOI-induced degeneracy breaking can account for this recurrence as well (see Supplementary Information section II and Extended Data Fig. 9) and remains the simplest explanation for the additional even Landau levels observed, though other effects such as strain[33,34] may contribute.

Induced SOI can additionally constrain the nature of the TBG phase diagram. Regardless of concrete SOI mechanism details, SOI acts as an explicit symmetry-breaking field that further promotes instabilities favoring compatible symmetry-breaking patterns while suppressing those that do not. For example, the relative robustness of the $\nu = 2$ correlated insulator in our $\theta = 0.97°$ device suggests that interactions favor re-populating bands[35,36] in a manner that also satisfies the spin-orbit energy. Furthermore, the survival of superconductivity with SOI constrains the plausible pairing channels—particularly given the dramatic spin-orbit-induced Fermi-surface deformations that occur at $\nu = +2$ (Fig. 4). Superconductivity in our low-twist-angle devices, for instance, is consistent with Cooper pairing of time-reversed partners that remain resonant with SOI. Thus the stability of candidate insulating and superconducting phases to the SOI provides additional nontrivial constraints for theory.[27,37–40] The integration of monolayer WSe_2 demonstrates the impact of the van der Waals environment and proximity effects on the rich phase diagram of TBG. In a broader context, this approach opens the future prospect of controlling the range of novel correlated phases available in TBG and similar structures by carefully engineering the surrounding layers, and it highlights a key tool for disentangling the mechanisms driving the different correlated states.

References:

1. Cao, Y. *et al.* Correlated insulator behaviour at half-filling in magic-angle graphene superlattices. *Nature* **556**, 80–84 (2018).

2. Cao, Y. *et al.* Unconventional superconductivity in magic-angle graphene superlattices. *Nature* **556**, 43–50 (2018).

3. Yankowitz, M. *et al.* Tuning superconductivity in twisted bilayer graphene. *Science* **363**, 1059–1064 (2019).

4. Sharpe, A. L. *et al.* Emergent ferromagnetism near three-quarters filling in twisted bilayer graphene. *Science* **365**, 605–608 (2019).

5. Lu, X. *et al.* Superconductors, orbital magnets and correlated states in magic-angle bilayer graphene. *Nature* **574**, 653–657 (2019).

6. Serlin, M. *et al.* Intrinsic quantized anomalous Hall effect in a moiré heterostructure. *Science* **367**, 900-903 (2019).

7. Stepanov, P. *et al.* The interplay of insulating and superconducting orders in magic-angle graphene bilayers. Preprint at https://arxiv.org/abs/1911.09198 (2019).

8. Saito, Y., Ge, J., Watanabe, K., Taniguchi, T. & Young, A. F. Decoupling superconductivity and correlated insulators in twisted bilayer graphene. Preprint at https://arxiv.org/abs/1911.13302 (2019).

9. Bistritzer, R. & MacDonald, A. H. Moiré bands in twisted double-layer graphene. *Proc. Natl. Acad. Sci. USA* **108**, 12233–12237 (2011).

10. Choi, Y. *et al.* Electronic correlations in twisted bilayer graphene near the magic angle. *Nat. Phys.* **15**, 1174–1180 (2019).

11. Polshyn, H. *et al.* Large linear-in-temperature resistivity in twisted bilayer graphene. *Nat. Phys.* **15**, 1011–1016 (2019).

12. Cao, Y. *et al.* Strange metal in magic-angle graphene with near Planckian dissipation. *Phys. Rev. Lett.* **124**, 076801 (2020).

13. Codecido, E. *et al.* Correlated insulating and superconducting states in twisted bilayer graphene below the magic angle. *Sci. Adv.* **5**, eaaw9770 (2019).

14. Kretinin, A. V. *et al.* Electronic properties of graphene encapsulated with different two-dimensional atomic crystals. *Nano Lett.* **14**, 3270–3276 (2014).

15. Zihlmann, S. *et al.* Large spin relaxation anisotropy and valley-Zeeman spin-orbit coupling in WSe_2/graphene/h-BN heterostructures. *Phys. Rev. B* **97**, 075434 (2018).

16. Island, J. O. *et al.* Spin–orbit-driven band inversion in bilayer graphene by the van der Waals proximity effect. *Nature* **571**, 85–89 (2019).

17. Wang, D. *et al.* Quantum Hall effect measurement of spin-orbit coupling strengths in ultraclean bilayer graphene/WSe_2 heterostructures. *Nano Lett.* **19**, 7028–7034 (2019).

18. Wakamura, T. *et al.* Spin-orbit interaction induced in graphene by transition metal dichalco-genides. *Phys. Rev. B* **99**, 245402 (2019).

19. Wilson, N. R. *et al.* Determination of band offsets, hybridization, and exciton binding in 2D semiconductor heterostructures. *Sci. Adv.* **3**, e1601832 (2017).

20. Kerelsky, A. *et al.* Maximized electron interactions at the magic angle in twisted bilayer graphene. *Nature* **572**, 95–100 (2019).

21. Xie, Y. *et al.* Spectroscopic signatures of many-body correlations in magic-angle twisted bilayer graphene. *Nature* **572**, 101–105 (2019).

22. Jiang, Y. *et al.* Charge order and broken rotational symmetry in magic-angle twisted bilayer graphene. *Nature* **573**, 91–95 (2019).

23. Koshino, M. *et al.* Maximally localized Wannier orbitals and the extended Hubbard model for twisted bilayer graphene. *Phys. Rev. X* **8**, 031087 (2018).

24. Lilly, M. P. *et al.* Resistivity of dilute 2D electrons in an undoped GaAs heterostructure. *Phys. Rev. Lett.* **90**, 056806 (2003).

25. Lee, P. A., Nagaosa, N. & Wen, X.-G. Doping a Mott insulator: Physics of high-temperature superconductivity. *Rev. Mod. Phys.* **78**, 17–85 (2006).

26. Wu, F., MacDonald, A. H. & Martin, I. Theory of phonon-mediated superconductivity in twisted bilayer graphene. *Phys. Rev. Lett.* **121**, 257001 (2018).

27. Lian, B., Wang, Z. & Bernevig, B. A. Twisted bilayer graphene: A phonon-driven supercon-ductor. *Phys. Rev. Lett.* **122**, 257002 (2019).

28. Wu, F., Hwang, E. & Das Sarma, S. Phonon-induced giant linear-in-T resistivity in magic angle twisted bilayer graphene: Ordinary strangeness and exotic superconductivity. *Phys. Rev. B* **99**, 165112 (2019).

29. Stewart, G. R. Heavy-fermion systems. *Rev. Mod. Phys.* **56**, 755–787 (1984).

30. Ardavan, A. *et al.* Recent topics of organic superconductors. *J. Phys. Soc. Japan* **81**, 011004 (2011).

31. Stewart, G. R. Superconductivity in iron compounds. *Rev. Mod. Phys.* **83**, 1589–1652 (2011).

32. Uri, A. *et al.* Mapping the twist angle and unconventional Landau levels in magic angle graphene. *Nature* **581**, 47—52 (2020).

33. Bi, Z., Yuan, N. F. Q. & Fu, L. Designing flat bands by strain. *Phys. Rev. B* **100**, 035448 (2019).

34. Zhang, Y.-H., Po, H. C. & Senthil, T. Landau level degeneracy in twisted bilayer graphene: Role of symmetry breaking. *Phys. Rev. B* **100**, 125104 (2019).

35. Zondiner, U. *et al.* Cascade of phase transitions and Dirac revivals in magic angle graphene. Preprint at https://arxiv.org/abs/1912.06150 (2019).

36. Wong, D. *et al.* Cascade of transitions between the correlated electronic states of magic-angle twisted bilayer graphene. Preprint at https://arxiv.org/abs/arXiv:1912.06145 (2019).

37. Guinea, F. & Walet, N. R. Electrostatic effects, band distortions, and superconductivity in twisted graphene bilayers. *Proc. Natl. Acad. Sci. USA* **115**, 13174–13179 (2018).

38. You, Y.-Z. & Vishwanath, A. Superconductivity from valley fluctuations and approximate SO(4) symmetry in a weak coupling theory of twisted bilayer graphene. *npj Quantum Mater.* **4**, 1–12 (2019).

39. Kozii, V., Isobe, H., Venderbos, J. W. F. & Fu, L. Nematic superconductivity stabilized by density wave fluctuations: Possible application to twisted bilayer graphene. *Phys. Rev. B* **99**, 144507 (2019).

40. Gu, X. *et al.* Antiferromagnetism and chiral d-wave superconductivity from an effective $t - J - D$ model for twisted bilayer graphene. Preprint at https://arxiv.org/abs/1902.00029 (2019).
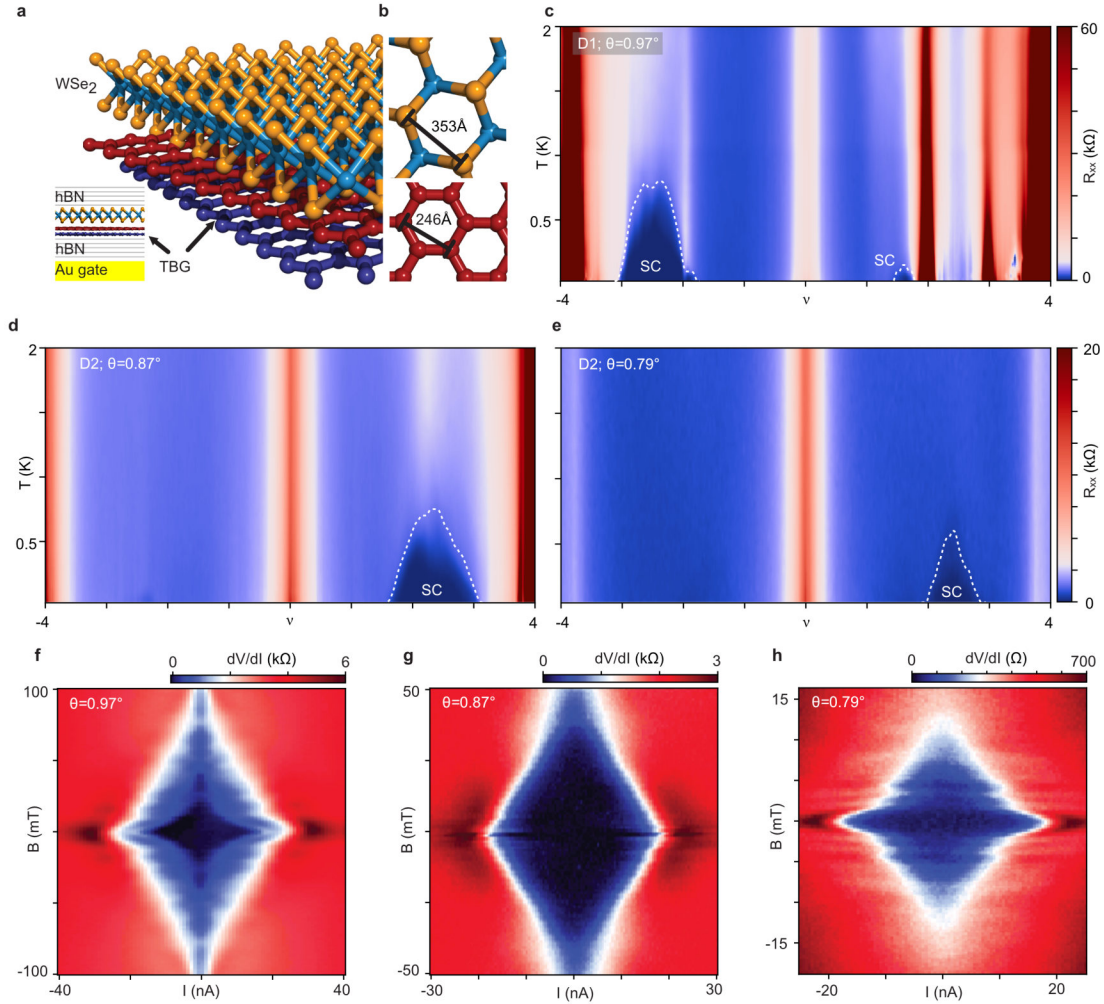
Figure 1 | Superconductivity in small-angle TBG-WSe$_2$ structures. a, Schematic of the TBG-WSe$_2$ structure showing the crystal lattice of two graphene layers (red and blue) and WSe$_2$ (yellow and cyan). Inset: Complete structure including encapsulating hBN layers on top and bottom and a gold back-gate. **b**, Top view of WSe$_2$ and graphene, indicating different unit-cell sizes. **c-e**, Longitudinal resistance R$_{xx}$ vs. temperature and electron density, expressed as a flat-band filling factor ν, for devices D1 and D2 and angles $\theta = 0.97°$, **c**; $\theta = 0.87°$, **d**; and $\theta = 0.79°$, **e**. In device D2, adjacent sets of electrodes have slightly different twist angle, as explained in the Methods section. Superconducting domes (SC) are indicated by a dashed line that delineates half of the resistance measured at 2 K (except for the electron-side dome for 0.97°, for which the normal temperature used was taken at 1K). **f-h**, Fraunhofer-like interference patterns, typically observed in TBG superconducting devices, for the three contact pairs ($\theta = 0.97°$, $\nu = -2.40$, **f**; $\theta = 0.87°$, $\nu = 1.96$ **g**; and $\theta = 0.79°$, $\nu = 2.30$, **h**).
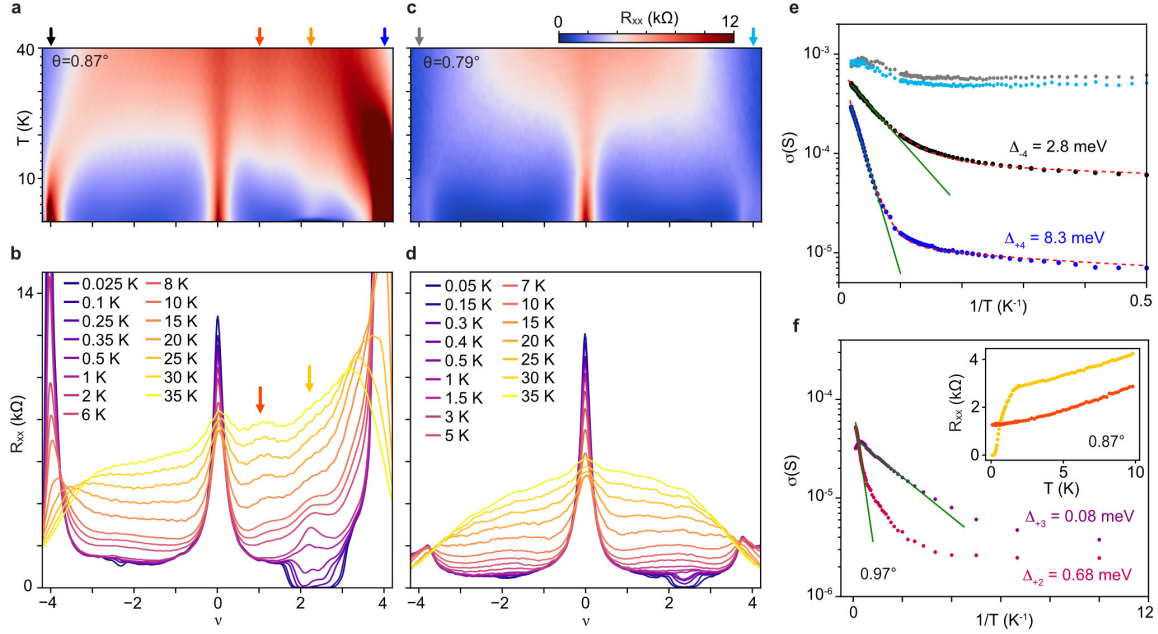
Figure 2 | Absence of correlated insulating states and diminished gap between flat and dispersive bands. a-d, Larger-temperature-range data showing R_{xx} as a function of filling factor ν, for θ = 0.87° (**a,b**) and θ = 0.79° (**c,d**). Line cuts shown in **b** (**d**) are taken from the same data set as **a** (**c**). **e,** Conductance vs. 1/T for full filling $\nu = \pm 4$ extracted from the data in **a** (blue and black) and **c** (cyan and gray). Green and red lines are fits for θ = 0.87° to a model that includes only activation (green) and both activation and variable-range hopping of the form $\exp[-(T_0/T)^{1/3}]$ (red).[41] The gap values shown are extracted from the activation-only fits (to the form of $\sigma \propto e^{-\Delta/2k_B T}$); the more complete model gives similar gap values of Δ_{+4} = 9.4 meV and Δ_{-4} = 3.7 meV. The behavior for θ = 0.79° shows much smaller variation in temperature. **f,** Conductance vs. 1/T for partial filling factors $\nu = +2, +3$ (shown with activated gap measurements) for 0.97° showing insulating behavior. In contrast, the inset shows that for 0.87°, partial fillings $\nu = \pm 2$ show metallic behavior.
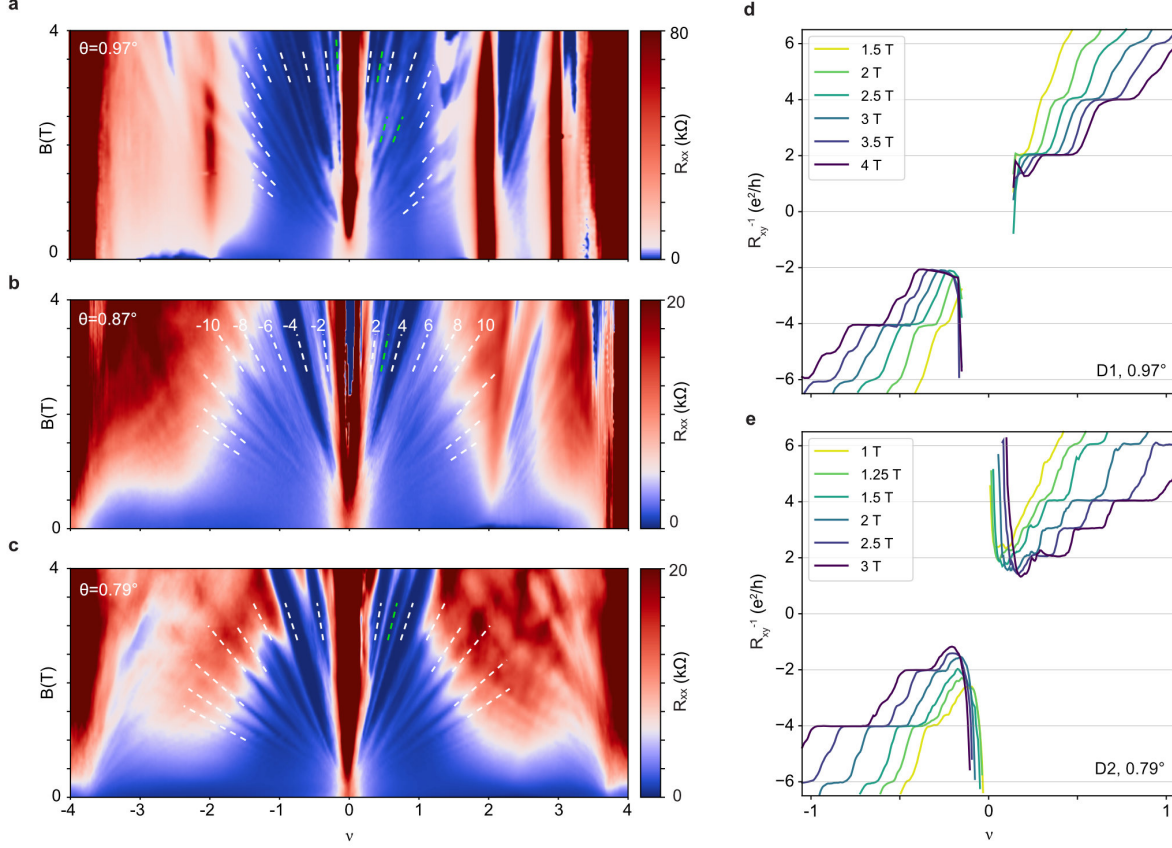
Figure 3 | Breaking of the four-fold degeneracy a-c, Longitudinal resistance R_{xx} as a function of magnetic field and ν for the three contacts pairs yielding $\theta = 0.97°$, $\theta = 0.87°$, and $\theta = 0.79°$. In contrast to typical hBN-TBG-hBN devices, here the dominant sequence in the Landau fan is ± 2, ± 4, ± 6, ± 8, ± 10, as labeled in **b**, indicating breaking of the four-fold (spin-valley) symmetry. After ± 10, we find a sequence of ± 14, ± 18, and ± 22, which can also be accounted for by SOC, as shown in Extended Data Fig. 9. Additional slopes are found in **a** corresponding to Landau levels -1, $+3$, -12, as well as short segments corresponding to $+5$ and $+7$ that disappear as the field increases. In **b, c** we find Landau level $+3$, but in **c** $+22$ seems to be missing. The odd levels are all marked with green lines. **d-e**, Hall conductance for devices D1 ($\theta = 0.97°$) and D2 ($\theta = 0.79°$) showing quantized steps around the CNP with steps corresponding to ± 2, ± 4 and ± 6 (in units of e^2/h) being pronounced down to 1.5 T. The less developed $3e^2/h$ step has also been observed. See Extended Data Fig. 2 for electrodes used in R_{xy} measurements. Measurements are performed at 20 mK.
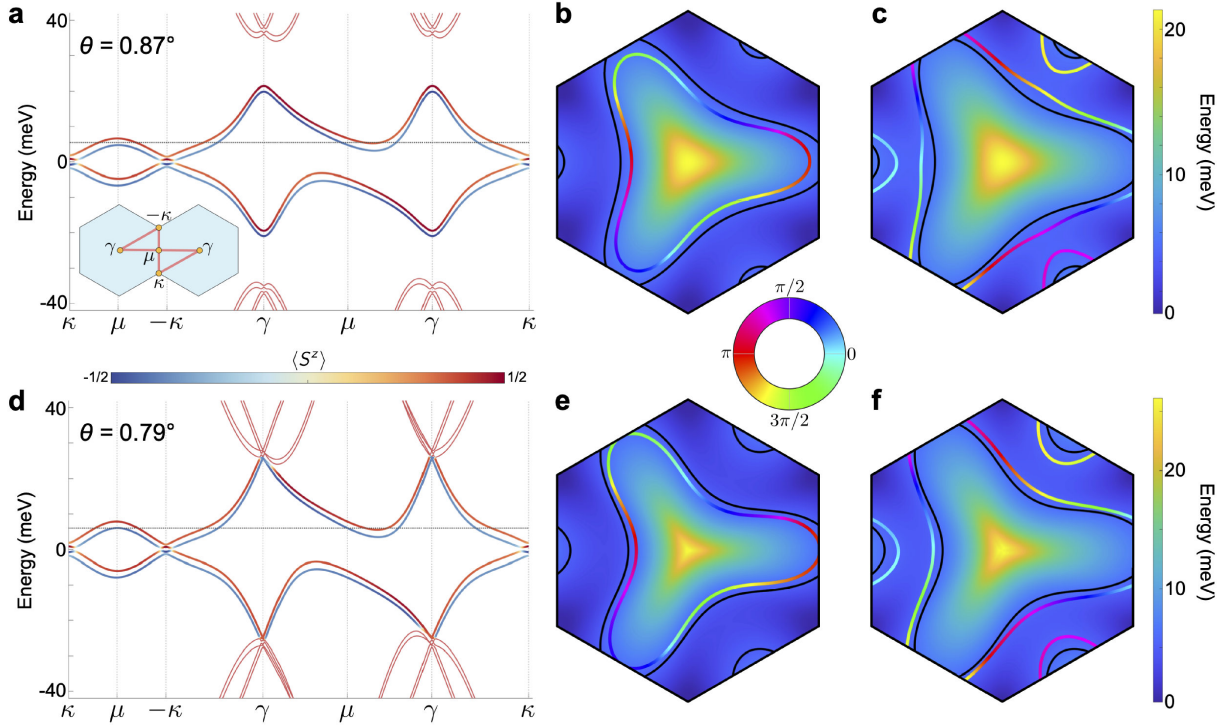
Figure 4 | Spin-orbit effect on TBG band structure Continuum-model results for valley K that include Ising and Rashba spin-orbit coupling at 0.87°(**a-c**) and 0.79°(**d-f**) twist angles. Details are given in the Methods and Supplementary Information section I. (**a, d**) Band structure along the high-symmetry directions of the Brillouin zone indicated in the inset. The line colour represents the out-of-plane spin projection, $\langle S_z \rangle$, and the dotted horizontal line denotes the chemical potential corresponding to $\nu = +2$. (**b,c**) and (**e, f**) Energy of the upper pair of flat conduction bands, including spin-orbit coupling. Coloured lines show the Fermi surfaces at $\nu = +2$, with the colour indicating the in-plane spin projection. The out-of-plane projection is largely constant along these surfaces and may therefore be deduced from **a** and **d**. Black lines correspond to the Fermi surface without SOI effects. The large spin-orbit-induced Fermi-surface deformation visible here reflects the flatness of the bands near the Fermi energy. The persistence of superconductivity with such distortions constrains the likely pairing channel in TBG. We note that the apparent electron-hole symmetry in the band structure is a consequence of twist angle being well below the magic-angle value.

Methods

Device Fabrication: The devices in this work were fabricated using a modified 'tear and stack' method; see Extended Data Fig. 1.[41,42] First, a thin hBN flake (7-15 nm) is picked up using a propylene carbonate film (PC) previously placed on a polydimethyl siloxane (PDMS) stamp. Then the hBN is used to pick an exfoliated monolayer of WSe_2 before approaching and 'tearing' the graphene. After picking up the first half of the graphene, the transfer stage is rotated by approximately 1.1-1.3° (overshooting the target angle slightly) and then the second half of the graphene is picked up, forming the TBG. Care was taken to approach each stacking step extremely slowly and at a high enough temperature (90°C) to minimise the formation of bubbles while avoiding the risk of twist-angle relaxation. See Extended Data Fig. 1 for a representative image of the stack on PC. In the last step, a thicker hBN (30-70 nm) is picked up, and the whole stack is dropped on a predefined local gold back-gate at 90°C while the PC is released at 165°C. The PC is then cleaned off with N-Methyl-2-Pyrrolidinone (NMP). The final geometry is defined by dry etching with a CHF_3/O_2 plasma and deposition of ohmic edge contacts (Ti/Au, 5 nm/100 nm); see Extended Data Fig. 1 for images of the finished devices and contacts pairs used in this study. We have used both commercial (HQ graphene) and lab-grown WSe_2 crystals (from University of Washington) and found no obvious difference in the resulting quality of devices.

Measurements: All measurements, unless otherwise specified, were performed in a dilution refrigerator (Oxford Triton) with a base temperature of 20 mK, using standard low-frequency lock-in amplifier techniques. The frequencies used on the lock-in amplifiers (Stanford Research, models 830 and 865a) were kept in the range of 7-23 Hz in order to measure the device's DC properties, and the AC excitation currents used were always < 5 nA, with most measurements taken at 100-500 pA to preserve the linearity of the system and avoid disturbing the fragile states at low temperatures. The fridge DC lines each pass through cold filters, including 4 Pi filters that filter out a range from ~ 80 MHz to >10 GHz, as well as a 2-pole RC low-pass filter. Unless otherwise specified, all measurements are taken at the base temperature.

Data Analysis: The twist angle between a pair of contacts was measured using the Landau fan diagram R_{xx} minima, from which we obtain the back gate voltage at charge neutrality as well as at the half- or full-filling voltage. Using this, and the fact that the slope of the Landau fan is directly proportional to the capacitance, the electron density at full filling (n_{full}) can be obtained. From the density, the twist angle is calculated using the low-angle approximation $\theta^2 \approx \sqrt{3}a^2 n_{full}/8$, where $a = 0.246$ nm is the lattice constant of graphene.[1] The conversion from back-gate voltage to filling factor ν (or electrons per Moiré unit cell) is then a linear transformation, where the electron(hole) full-filling voltage corresponds to $\nu = +(-)4$. The twist-angle determination using this method is accurate to $\pm 0.01°$.

Possible mechanisms for stabilizing superconductivity: In comparison to previous studies,[2,3,5,7,8] the main difference in our samples originates from the addition of a WSe_2 monolayer. There are several possible reasons why this change stabilizes superconductivity at smaller angles. For example, details of the microscopic interface between graphene and hBN (or WSe_2) could result

in differing friction coefficients, which could play an important role in setting the angle disorder distribution during the fabrication process. While other details of fabrication have a significant impact, we have observed less angle disorder in the samples where WSe$_2$ was used to pick up the TBG. Various effects can also arise from having different interfaces on the two sides of the TBG due to differences in the moiré patterns or built-in electric fields. However, these effects can be partly ruled out by encapsulating TBG with WSe$_2$ on both sides, which we have shown in Extended Data Fig. 7. More fundamentally, WSe$_2$ could affect the overall electronic band structure and density of states through modifications of interlayer coupling in TBG, induced SOI, renormalization of Fermi velocity, and other factors. It is likely that a combination of these band-structure-related effects is essential for stabilizing superconductivity down to the angles studied here.

Choice of model parameters

The model calculations of the TBG band structure in Fig. 4 are based on the continuum model[9] plus induced spin-orbit coupling in one of the graphene monolayers; the model is discussed in detail in Supplementary Information section I. The parameters used are $(w_0, w_1) = (55, 105)$ meV and spin-orbit parameters $(\lambda_I, \lambda_R, \lambda_{\mathrm{KM}}) = (3, 4, 0)$ meV. The velocity of the graphene monolayers is left unaltered from the value provided above: $v_0 \sim 10^6$ m/s. This set of parameters both returns magic-angle values of $\theta = 1° - 1.1°$ and quantitatively reproduces the twist angle dependence of the gap on the electron side (within $30 - 50\%$).

Velocity and interlayer tunnelling: Our choice of w_0 deviates slightly from those reported in the literature,[9, 43–45] but does not alter the magic angle value substantially, which is primarily controlled through w_1. The relative weakness of the w_0 used here compared to the values found in the literature may be ascribed to the greater importance of lattice relaxation at smaller twist angles.

The choice to leave v_0 (t), w_1, and, as a result, the magic angle relatively unchanged compared to hBN-encapsulated TBG systems has been made for simplicity. In principle, the proximity to transition metal dichalcogenide layer could alter these parameters as well. For instance, Ref. 46 finds that the nearest-neighbour hopping energy t of the top graphene monolayer should be reduced to 2.5 eV from 2.6 eV (implying a reduction in v_0 on the top layer). Similarly, the presence of WSe$_2$ may also change the interlayer tunnelling parameters, w_0 and w_1. As the magic angle is largely controlled through the parameter $\alpha = w_1/(\hbar v_0 k_\theta) \propto w_1/(\hbar v_0 \theta)$,[9] such modifications could shift the location of the magic angle. However, experimentally, we have observed correlated insulating states to be pronounced around 0.97°– 1.04°, similar to the previous work[1] indicating that the magic-angle condition is not changed substantially (on the scale of angles considered in this work). We note that screening effects which may be different due to WSe$_2$ may play a role in suppressing correlated insulating states.[47, 48]

Spin-orbit parameters: The values of the spin-orbit parameters deduced from magnetic field measurements in Extended Data Fig. 8 ($\sim$1 meV) and those used in our modeling of the band structure and Landau levels ($\sim$3-4 meV) are both consistent with the values reported in the literature (0.5-15 meV) for monolayer and bilayer graphene.[15–18, 49, 50] The apparent difference of 3-4 in

SOI strength may easily arise due to several factors including not accounting for strain in model calculations and using an expression for single layer graphene in the weak antilocalization fits. While most of the theoretical[46,51,52] and experimental[15–17,49,50] work does not include or explicitly rule out Kane-Mele SOI in graphene proximitized with WSe_2, the recent work described in Ref. 18 argues that this term is dominant sufficiently close to charge neutrality. Since both Ising and Kane-Mele terms contribute similarly to the spin relaxation times,[50] and the band structure of TBG is more complex in comparison to monolayer and bilayer graphene, it is challenging to distinguish their separate contribution in our weak antilocalization measurements. The effect of different SOI terms is shown in Extended Data Fig. 10, where the band structure is shown with Ising, Rashba, and Kane-Mele SOI terms separately nonzero.

Data availability: The data that support the findings of this study are available from the corresponding authors on reasonable request.

Additional References:

41. Cao, Y. *et al.* Superlattice-induced insulating states and valley-protected orbits in twisted bilayer graphene. *Phys. Rev. Lett.* **117**, 116804 (2016).

42. Kim, K. *et al.* Van der Waals heterostructures with high accuracy rotational alignment. *Nano Lett.* **16**, 1989–1995 (2016).

43. Nam, N. N. T. & Koshino, M. Lattice relaxation and energy band modulation in twisted bilayer graphene. *Phys. Rev. B* **96**, 075311 (2017).

44. Po, H. C., Zou, L., Vishwanath, A. & Senthil, T. Origin of Mott insulating behavior and superconductivity in twisted bilayer graphene. *Phys. Rev. X* **8**, 031089 (2018).

45. Carr, S., Fang, S., Zhu, Z. & Kaxiras, E. Exact continuum model for low-energy electronic states of twisted bilayer graphene. *Phys. Rev. Res.* **1**, 013001 (2019).

46. Gmitra, M., Kochan, D., Högl, P. & Fabian, J. Trivial and inverted Dirac bands and the emergence of quantum spin Hall states in graphene on transition-metal dichalcogenides. *Phys. Rev. B* **93**, 155104 (2016).

47. Goodwin, Z. A. H., Corsetti, F., Mostofi, A. A. & Lischner, J. Twist-angle sensitivity of electron correlations in moiré graphene bilayers. *Phys. Rev. B* **100**, 121106 (2019).

48. Pizarro, J. M., Rösner, M., Thomale, R., Valentí, R. & Wehling, T. O. Internal screening and dielectric engineering in magic-angle twisted bilayer graphene. *Phys. Rev. B* **100**, 161102 (2019).

49. Wang, Z. *et al.* Origin and magnitude of 'designer' spin-orbit interaction in graphene on semiconducting transition metal dichalcogenides. *Phys. Rev. X* **6**, 041020 (2016).

50. Cummings, A. W., Garcia, J. H., Fabian, J. & Roche, S. Giant spin lifetime anisotropy in graphene induced by proximity effects. *Phys. Rev. Lett.* **119**, 206601 (2017).

51. Gmitra, M. & Fabian, J. Graphene on transition-metal dichalcogenides: A platform for proximity spin-orbit physics and optospintronics. *Phys. Rev. B* **92**, 155403 (2015).

52. Li, Y. & Koshino, M. Twist-angle dependence of the proximity spin-orbit coupling in graphene on transition-metal dichalcogenides. *Phys. Rev. B* **99**, 075438 (2019).

53. Wang, Z. *et al.* Strong interface-induced spin-orbit interaction in graphene on WS_2. *Nat. Comm.* **6**, 8339 (2015).

54. McCann, E. & Fal'ko, V. I. $z \rightarrow -z$ symmetry of spin-orbit coupling and weak localization in graphene. *Phys. Rev. Lett.* **108**, 166606 (2012).

Author Contribution: H.A., R.P., Y.Z., and S.N.-P. designed the experiment. H.A. made the TBG-WSe_2 devices assisted by Y.Z., H.K. and Y.C. H.A. and R.P., performed the measurements. Y.Z. made and measured initial TBG devices and D4. H.A., R.P., and S.N.-P. analyzed the data. A.T. and J.A. developed the continuum model that includes spin-orbit interaction and performed model calculations. Z.L., I.Z.W., X.X., and J.-H.C. provided WSe_2 crystals. K.W. and T.T. provided hBN crystals. H.A., R.P., Y.Z., A.T., J.A., and S.N.-P. wrote the manuscript with input from other authors. S.N.-P. supervised the project.

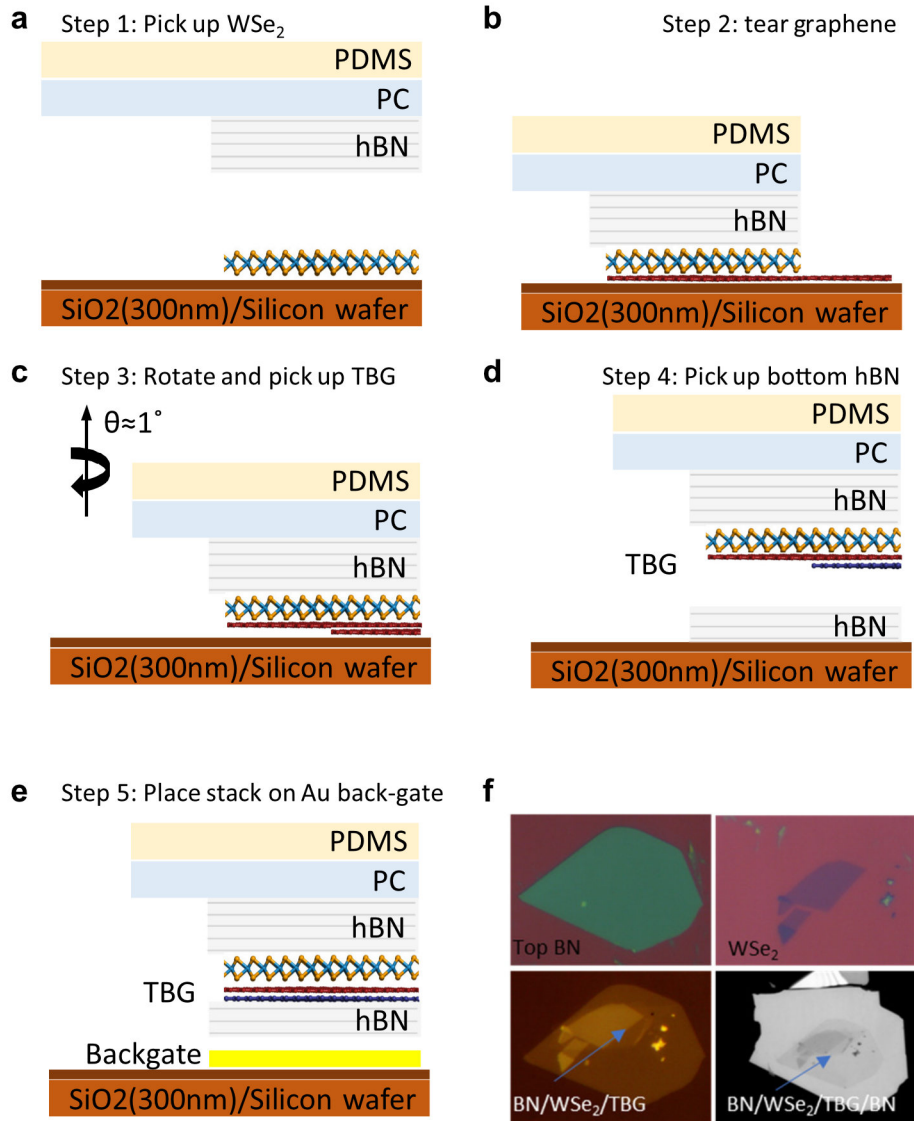**Competing interests:** The authors declare no competing interests.

Additional Information

**Supplementary Information** is available for this paper online.

Correspondence and requests for materials should be addressed to S.N.-P.

**Reprints and permissions information** is available at http://www.nature.com/reprints

Extended data figure legend:

a Step 1: Pick up WSe$_2$

PDMS
PC
hBN

SiO2(300nm)/Silicon wafer

b Step 2: tear graphene

PDMS
PC
hBN

SiO2(300nm)/Silicon wafer

c Step 3: Rotate and pick up TBG

θ≈1˚

PDMS
PC
hBN

SiO2(300nm)/Silicon wafer

d Step 4: Pick up bottom hBN

PDMS
PC
hBN
TBG

hBN

SiO2(300nm)/Silicon wafer

e Step 5: Place stack on Au back-gate

PDMS
PC
hBN
TBG
hBN
Backgate

SiO2(300nm)/Silicon wafer

f

Top BN   WSe$_2$

BN/WSe$_2$/TBG   BN/WSe$_2$/TBG/BN

Extended Data Figure 1 | Fabrication details a-e, Critical steps in the stacking process. **f**, Optical images of a typical flakes and stacks at different stages of the fabrication.

18
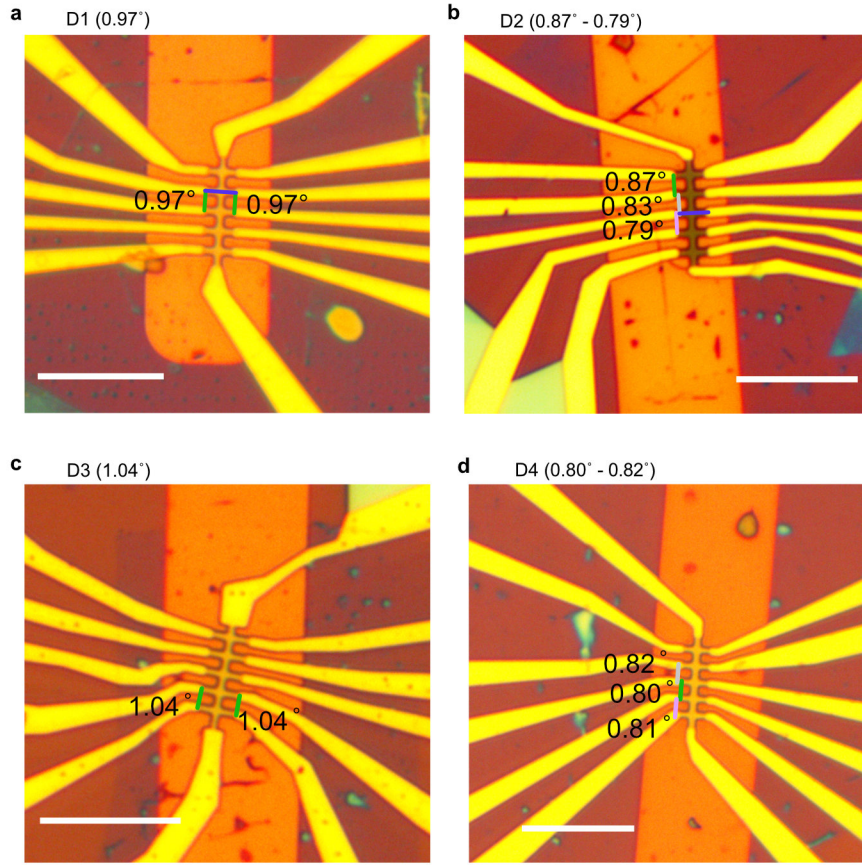
Extended Data Figure 2 | Optical images of devices D1-D4 Electrodes that are used in the measurements and corresponding twisted angles are labeled for each device. The ones marked with blue lines are used for measuring Hall conductance in Fig. 3. The scale bar in each panel corresponds to 15 μm. The device bottom hBN thicknesses for D1, D2, D3, and D4 are 62 nm, 40 nm, 48 nm, and 56 nm, respectively. D4 differs from the other devices since it features monolayer WSe$_2$ on both the top and bottom of the device. The contact angle, for each pair of contacts listed, were determined from the Landau fan diagrams, as described in Methods.
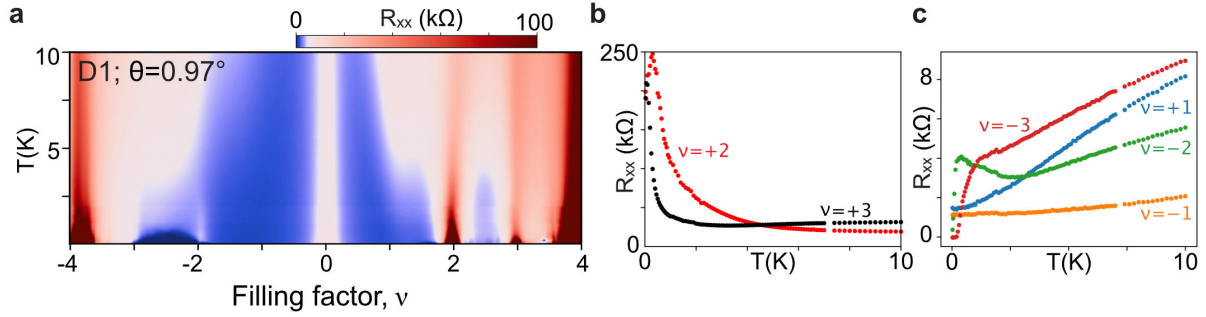
Extended Data Figure 3 | Additional temperature data for device D1 (0.97°) a, R_{xx} as a function of ν and Temperature up to 10 K. **b,** Temperature dependence of R_{xx} for $\nu = 2$ and $\nu = 3$ showing insulating behaviour. **c,** At other partial integer filling factors R_{xx} increases with temperature, consistent with metallic behaviour.
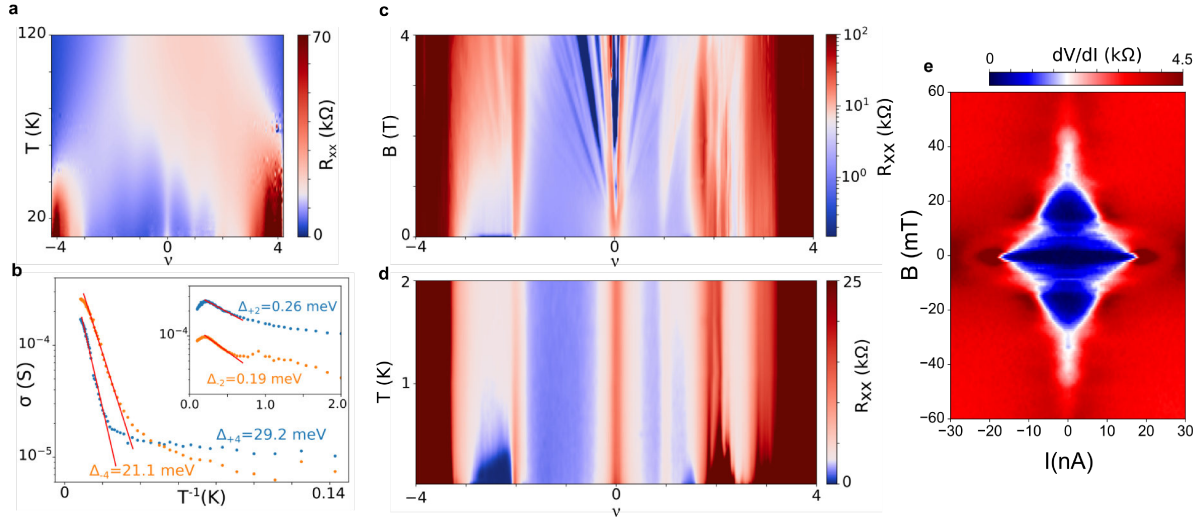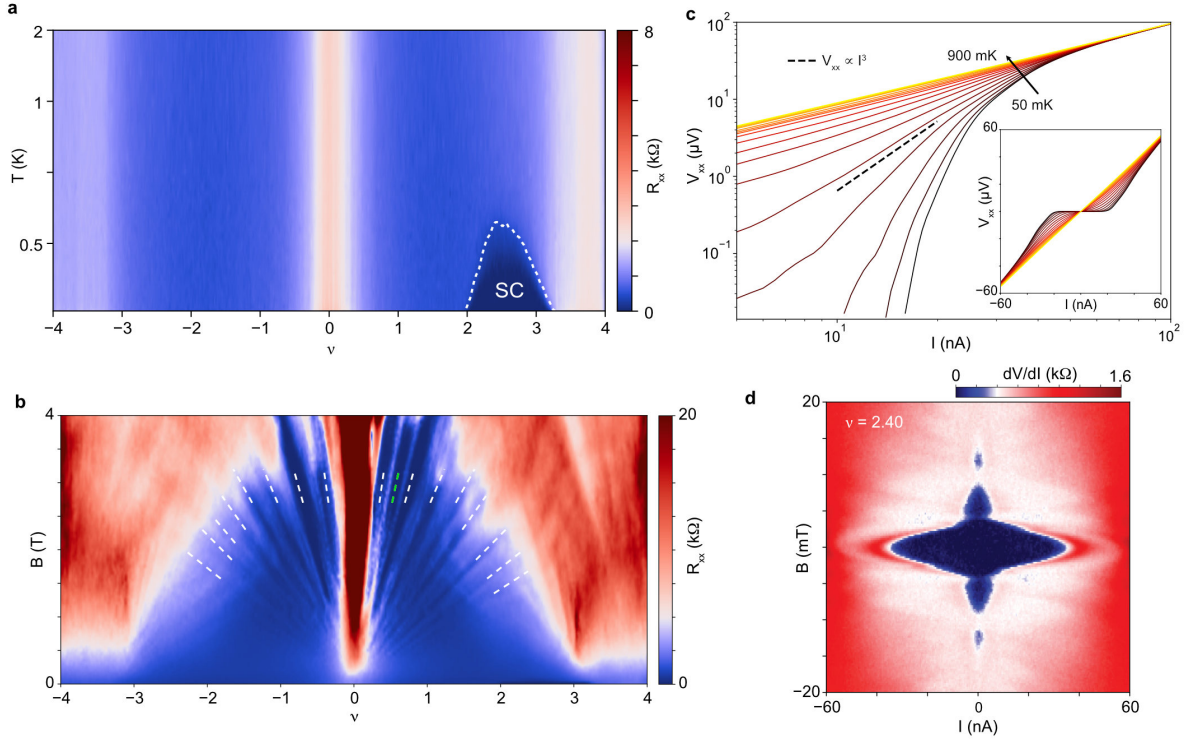
Extended Data Figure 4 | Additional data for device D3 (1.04°) a, R_{xx} as a function of ν and temperature up to 120 K. In this device, a higher temperature was required for fitting the Arrhenius gaps, due to the larger gap size. Thus, the panel **a** data was measured in a variable temperature (Quantum Design PPMS) setup, while data from other panels were taken in the dilution fridge. **b**, Line cuts from panel a, with corresponding fits showing gaps at full filling $\Delta_{\pm4}$ and partial filling $\Delta_{\pm2}$. **c**, Landau fan diagram showing similar behaviour as D1(0.97°). **d**, Temperature dependence up to 2 K clearly showing superconductivity on the hole side (for $-3 < \nu < -2$) and smaller pocket on the electron side showing signatures of developing superconductivity. **e**, Fraunhofer-like pattern at ν = -2.78.
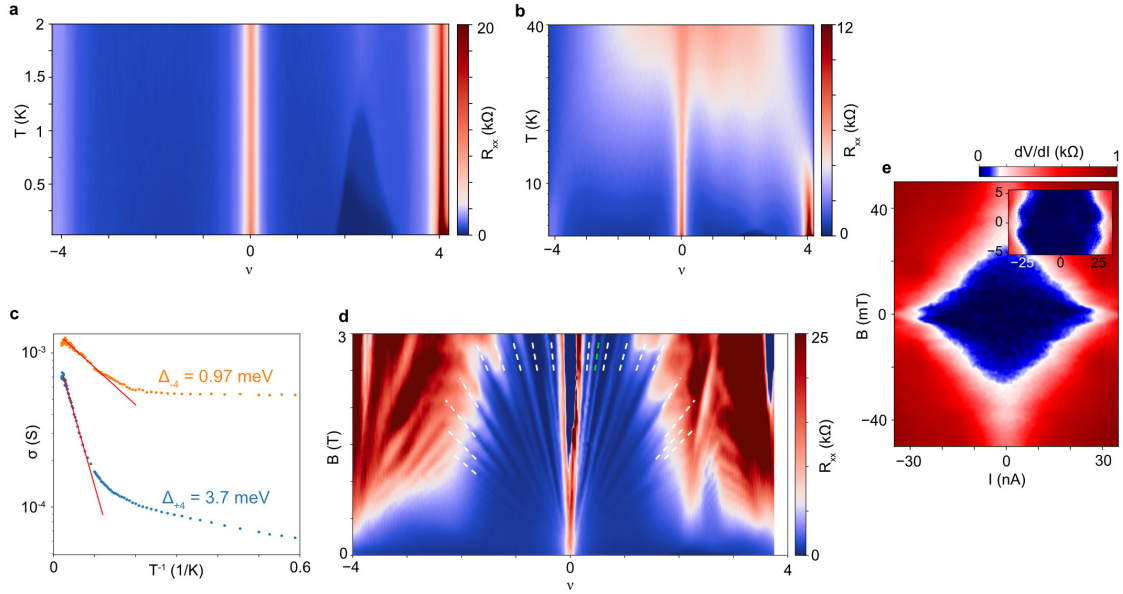
Extended Data Figure 5 | Additional data for device D2, 0.83°contacts See Extended Data Fig. 2b for the layout of D2. **a**, R_{xx} plotted for filling factor ν and temperature to 2 K, showing the superconducting pocket on the electron side. **b**, Same up to 40 K, showing the reduction of the $|\nu|$ = 4 insulating states and **c** Arrhenius fits to the gap values of 0.97 meV for $\nu = -4$ and 3.7 meV for $\nu = +4$. **d** R_{xx} vs. filling factor and magnetic field (B), forming a Landau fan diagram, with white dashed lines tracing the dominant ± 2, $+3$, ± 4, ± 6, ± 8, ± 10, ± 14, ± 18, $+20$, ± 22, -26 sequence around charge neutrality. The odd level ($+3$) is marked with green. **e** The Fraunhofer-like pattern for the superconductivity pocket, taken at $\nu = 2.08$. The inset is a zoom into the low-field data, showing that the critical current reaches a local minimum about 0 field indicating a "π"-junction like behaviour.[3]
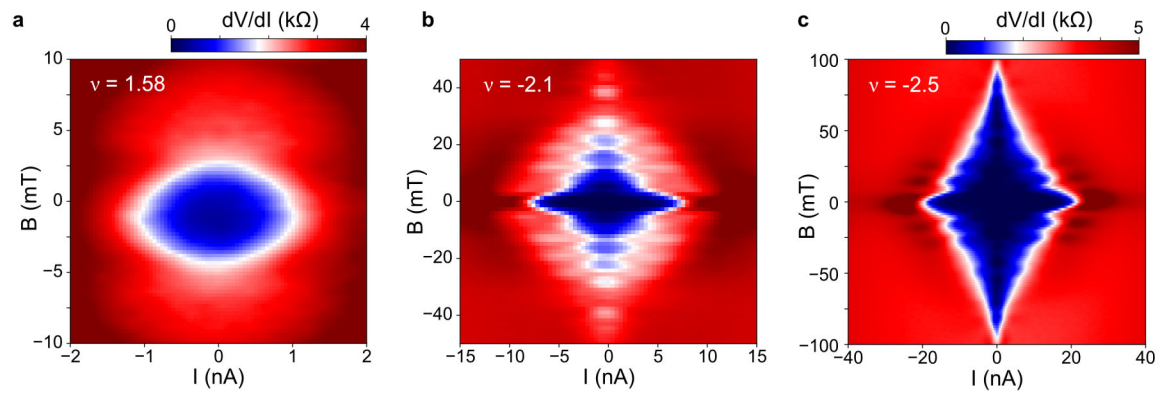
Extended Data Figure 6 | Additional data from device D1 (0.97°) a, Fraunhofer-like pattern for electron doping, at $\nu = 1.58$. **b, c,** Additional Fraunhofer-like pattern for hole doping, $\nu = -2.1$ (**b**), and $\nu = -2.5$ (**c**).

Extended Data Figure 7 | Additional data for device D4 (0.80°) D4 was fabricated with mono-layer WSe_2 on both the top and bottom of the TBG. **a**, R_{xx} as a function of ν and temperature to 2 K, revealing a superconducting pocket over the range of $2 < \nu < 3.2$ and resistance at full filling ($\nu = |4|$) less than at the charge neutrality point. **b**, The Landau fan, with dotted lines drawn from the charge neutrality point according to the sequence ±2, $+3$, ±4, ±6, ±8, ±10, -12, ±14, ±18, $+22$, with the odd level ($+3$) marked in green. **c**, Current vs. voltage at $\nu = 2.79$, at temperatures from 50 mK to 900 mK, in 50 mK steps. The main plot is on the log scale in both axes, revealing a BKT transition temperature near 250 mK. Inset: I-V dependence for the same temperatures. **d**, Fraunhofer-like pattern for D4 at $\nu = 2.40$.
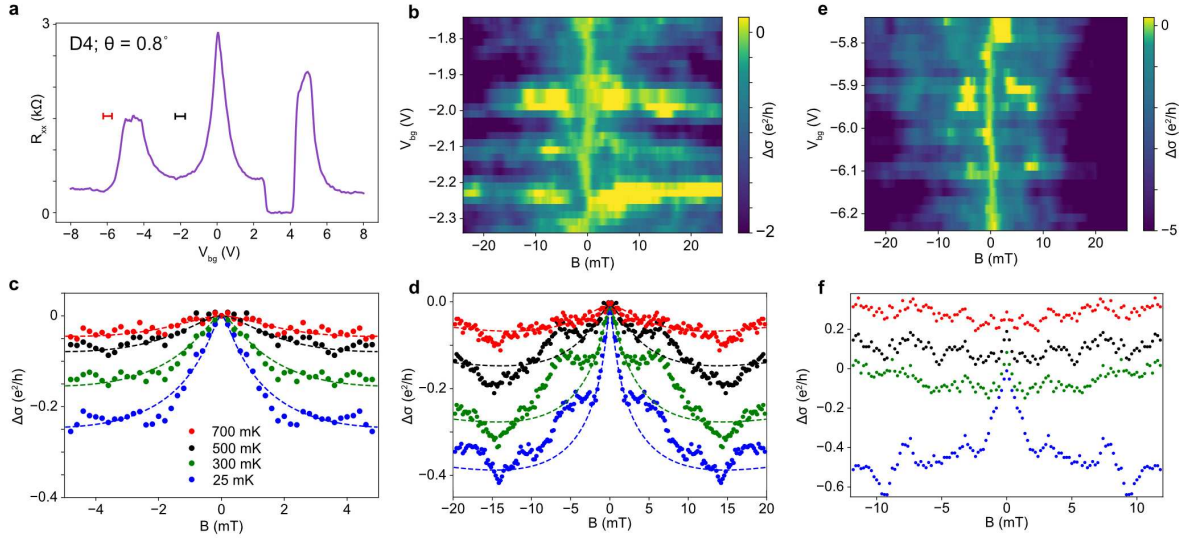
Extended Data Figure 8 | Weak Antilocalization (WAL) data measured in D4 ($\theta = 0.80°$) a, R_{xx} as a function of backgate voltage, V_{bg}, for the 0.80° contacts of D4 (see Extended Data Fig. 2). The black(red) line shows the voltage range used in the flat(dispersive) bands, which corresponds to the plots in **b-d(e, f)**. The peak at B = 0 mT is prominent in both ranges, showing the presence of weak antilocalization and consequently spin-orbit coupling. **b**, The change in conductivity, relative to the 0 mT point, as a function of magnetic field ($\Delta\sigma$) taken at several gate voltages in the range of V_{bg} $\approx$ –2 V measured at 25 mK; the narrow peak about B = 0 mT, indicative of WAL, is clearly visible. Universal conductance fluctuations, can be averaged out by taking field sweeps at different gate points.[53] **c, d,** averaged data from **b** for different field ranges. The data taken at 900 mK—where the WAL peak has disappeared—has been subtracted, and the data points have been symmetrized about 0 mT. The dashed lines are the comparison with the model[54] used previously for monolayer graphene/transition metal dichalcogenides heterostructures[18,53] with a renormalized Fermi velocity to account for the flatness of the bands. For generating plots at different temperatures, only the dephasing scattering time τ_ϕ is varied. Whereas the total spin-orbit scattering time $\tau_{so} \approx 10$ ps better reproduces the low-field data in **c**, $\tau_{so} \approx 1$–3 ps captures the saturation at larger fields (**d**) with asymmetric and symmetric relaxation time ratio[54] (τ_{asym}/τ_{sym}) varying in range 0.3–3. The values of τ_{so} obtained here correspond to SOI energies[50] in the range of 0.5–1 meV. We note that, in the case of TBG, a more detailed analysis with a correct model for describing WAL in TBG is likely required for quantitative comparison. Regardless, the WAL peaks are an indication of strong SOI in WSe$_2$/TBG heterostructures. The data in (**e, f**) show a WAL peak in the dispersive bands near $V_{bg} = -6$V (red line in **a**). Data in (**e**) was taken at 25 mK. In (**f**), the data points at each temperature are offset by 0.1 e^2/h for clarity.
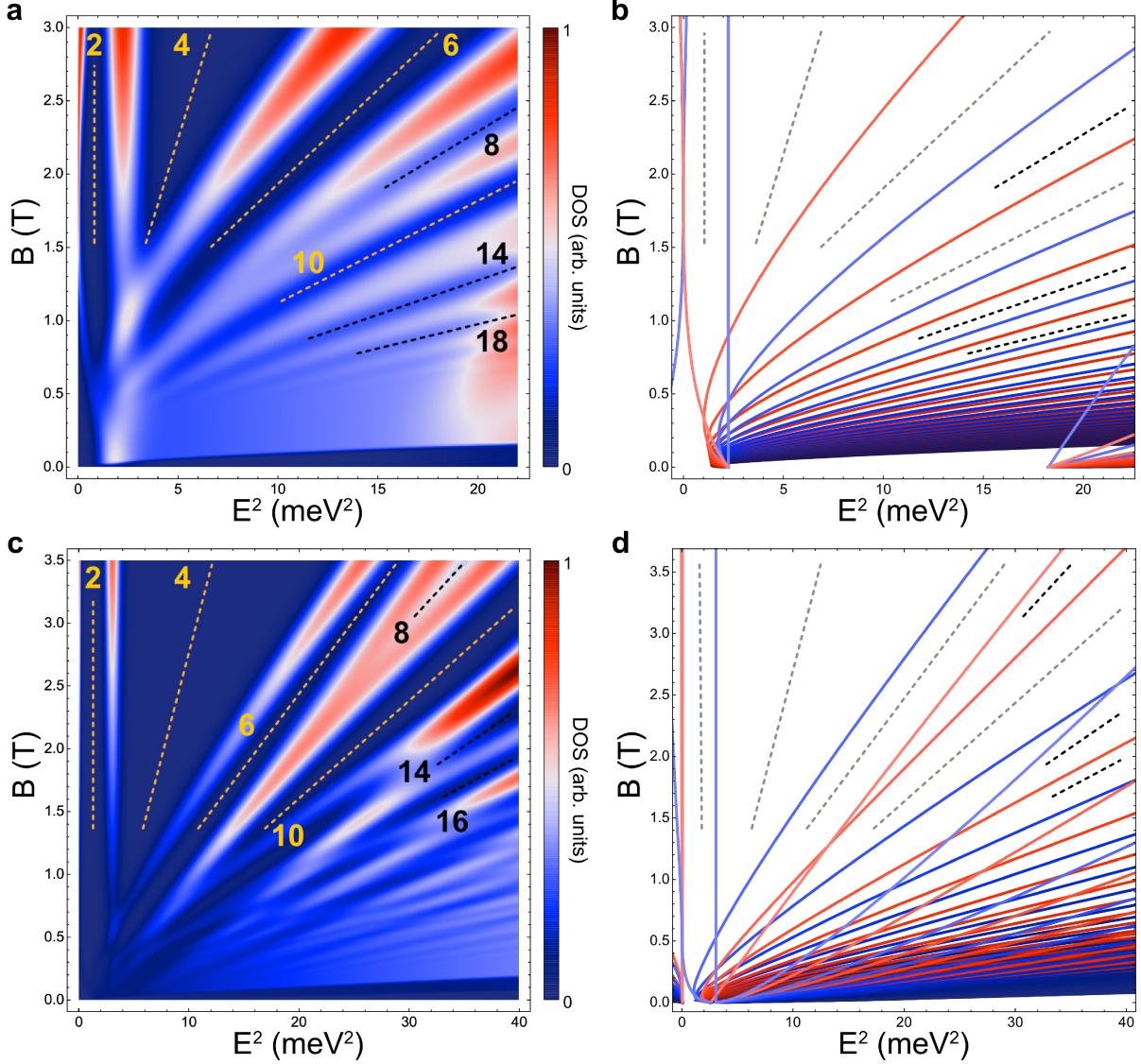
Extended Data Figure 9 | Theoretical Landau-level spectrum. (**a**, **c**) Colour plot of the phenomenologically broadened density of states (see Supplementary Information section II for details) as a function of energy squared in $(\text{meV})^2$ (roughly equivalent to the electron density that is gate-tuned in the experiment) and the magnetic field in Tesla. (**b**, **d**) The spectrum without taking broadening effects into account. Blue and red lines correspond to levels originating proximate to the $+\mathbf{K}$ and $-\mathbf{K}$ valleys respectively. The parameters considered are $(\tilde{\lambda}_I, \tilde{\lambda}_R, \tilde{\lambda}_{\text{KM}}) = (3, 4, 0)$ meV with a broadening $\Gamma = 0.22$ meV and (**a**, **b**) and $(\tilde{\lambda}_I, \tilde{\lambda}_R, \tilde{\lambda}_{\text{KM}}) = (1.5, 2.5, 2)$ meV with a broadening $\Gamma = 0.15$ meV (**c**, **d**). The velocity in both is $v_F \approx 10^5$ m/s, as is appropriate for $\theta \approx 0.8° - 0.9°$. We note that the Landau level sequence and energy levels on the hole-doped side are identical to those shown here for **a** and **b**. When both $\tilde{\lambda}_I$ and $\tilde{\lambda}_{\text{KM}}$ are nonzero, as in **c** and **d**, a slightly different Landau-level sequence is generically obtained at negative energies relative to the CNP.
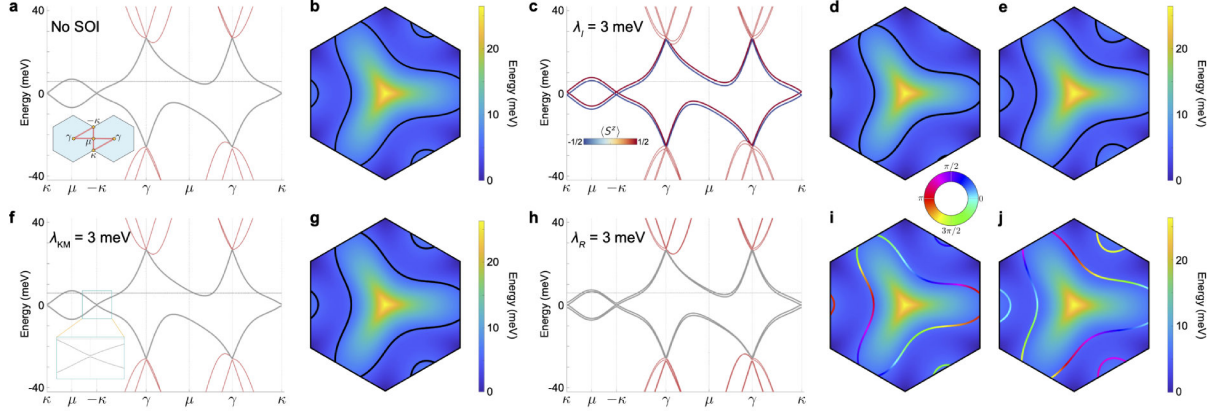
Extended Data Figure 10 | SOI-dependence of band structure (**a**, **c**, **f**, **h**) Flat-band energies along momentum line cuts defined in the inset of (**a**); dashed lines indicate the chemical potential corresponding to $\nu = +2$. (**b**, **d**, **e**, **g**, **i**, **j**) Band structure of the electron-like bands with their $\nu = +2$ Fermi surfaces indicated, for different values of the SOI parameters. We consider the cases where no SOI is present (**a**, **b**), and where only Ising (**c-e**), only Kane-Mele (**f**, **g**), and only Rashba (**h-j**) SOI are present. In **c-j**, the non-zero SOI parameter is set to 3 meV; other parameters are provided in the Methods. In **c**, the bands possess an out-of-plane spin polarization ($\langle S^z \rangle$), which is displayed in colour as per the inset. As indicated in Fig. 4, when both λ_I and λ_R are non-zero, the Dirac cones at $\pm\kappa$ generate masses. In contrast, when λ_I, λ_R, λ_{KM} are individually the only non-zero SOI, only the Kane-Mele term results in a gapped spectrum at charge neutrality. In **f**, the inset zooms in on the $-\kappa$ point to demonstrate this point. Aside from this feature, the band structure when $\lambda_{\text{KM}} = 3$ meV (**h**, **g**) is qualitatively identical to the band structure without SOI (**a**, **b**). In **i** and **j**, the colour of the Fermi surfaces indicates the expectation value of the in-plane spin according to the wheel above **i**. All other parameter sets have a zero in-plane spin projection.